

## OH-SELECTED AGB AND POST-AGB STELLAR OBJECTS. II. BLUE VERSUS RED EVOLUTION OFF THE AGB

MAARTJE N. SEVENSTER<sup>1</sup>

MSSSO/RSAA, Cotter Road, Weston ACT 2611, Australia

*Draft version October 27, 2018*

### ABSTRACT

Using objects found in a systematic survey of the galactic Plane in the 1612-MHz masing OH line, we discuss in detail two “sequences” of post-AGB evolution, a red and a blue. We argue that the red and the blue groups separate by initial mass at  $M_i=4 M_\odot$ , based on evolutionary-sequence turn-off colours, spectral energy distributions, outflow velocities and scaleheight. The higher-mass (blue) objects may have earlier AGB termination. The lower-mass (red) objects undergo very sudden reddening for IRAS colour  $R_{21}\sim 1.2$ ; these sources must all undergo a very similar process at AGB termination. The transition colour corresponds to average initial masses of  $\sim 1.7 M_\odot$ . The combined colour  $2.5 \log((S_{21}^{\text{msx}} S_{12}^{\text{iras}})/(S_8^{\text{msx}} S_{25}^{\text{iras}}))$  proves very sensitive to distinguish lower-mass, early post-AGB objects from sources still on the AGB and also to distinguish more evolved post-AGB objects from star-forming regions. The high-mass blue objects are the likely precursors of bipolar planetary nebulae, whereas the low-mass red objects will evolve into elliptical planetary nebulae.

*Subject headings:* Stars:AGB and post-AGB – Stars:evolution – planetary nebulae

### 1. INTRODUCTION

Maser emission in the satellite line of groundstate OH at 1612.231 MHz occurs in a variety of stellar objects. Star-forming regions (SFR), super giants, visible (Miras) and invisible (OH/IR) oxygen-rich stars at the tip of the asymptotic giant branch (AGB) and post-AGB transition objects or even young planetary nebulae can all show maser emission at 1612 MHz. Spectral shapes and variability are thought to differ for the several different types of object, but in Paper I (Sevenster 2002), the OH spectral properties were found to vary less clearly with evolutionary state than usually assumed. New selection criteria for post-AGB objects were defined, based largely on mid-infrared colours from the Midcourse Space Experiment (MSX). Most post-AGB objects are distinguished by very red mid-infrared colours, but there is also a group of very blue sources with a strong 60- $\mu\text{m}$  excess. These sources are not on the oxygen-rich AGB evolutionary sequence (see Section 2) and are possible post-AGB sources according to van der Veen & Habing (1988).

In this paper, this group of objects will be compared to the standard red post-AGB objects and properties of both groups will be discussed. We will use 56 objects from the same sample<sup>2</sup> as in Paper I, of OH-masing sources in the galactic Plane (Sevenster et al. 1997a, 1997b, 2001) with IRAS (12, 25, 60, 100  $\mu\text{m}$ ), MSX (4, 8, 12, 15, 21  $\mu\text{m}$ ) and 2MASS identifications (J, H, K) taken from the respective public databases (see Paper I for details). A relatively small percentage of IRAS identifications is caused largely by (cirrus) confusion at the very low latitudes of our survey ( $|b| < 3^\circ.25$ ). For the same reason, the flux-density measurements, especially at 60  $\mu\text{m}$  and 100  $\mu\text{m}$ , are likely to be somewhat overestimated even if they are not flagged as “upper limits” in the IRAS data base. Except for a few likely supergiants, none of the sources were identified with

an optical counterpart.

In Section 2, we define the two groups of post-AGB stars in more detail and, in Section 3, discuss some evolutionary aspects. Spectral energy distributions are given in Section 4 and compared to classes of post-AGB stars defined previously in the literature. In Section 5, age, luminosity and galactic distribution of the two groups are discussed and put in the context of planetary nebula morphology. Conclusions are listed in Section 6.

### 2. THE TWO POST-AGB SAMPLES

All mid-infrared (MIR) colours are defined as  $[a - b] = 2.5 \log(S_b/S_a)$  with  $S$  flux density in Jy and a, b wavelength in  $\mu\text{m}$ . For IRAS, the usual names  $R_{21} \equiv [12 - 25]$  and  $R_{32} \equiv [25 - 60]$  are used, as well as  $R_{43} \equiv [100 - 60]$ . IRAS magnitudes  $[12] \equiv 2.5 \log(59.5/S_{12})$  and  $[25] \equiv 2.5 \log(13.4/S_{25})$  are also used. For more details on the different bands, see Paper I. From the 2MASS database, J (1.25  $\mu\text{m}$ ), H (1.65  $\mu\text{m}$ ) and/or K (2.17  $\mu\text{m}$ ) magnitudes were obtained for 194 sources. Colours are used as uncorrected J-H and H-K.

The two groups of post-AGB stars are defined as follows. The blue group, called “LI” for lying to the left of the evolutionary sequence in the IRAS diagram (see Fig. 1), are selected by  $R_{32} > -0.2$  and  $R_{21} > 0.2$ , with

$$R_{32} > -2.15 + 0.35 \exp[1.5 R_{21}] \quad (1)$$

the evolutionary sequence according to van der Veen & Habing (1988). Van der Veen & Habing (1988) show that this region in the IRAS colour-colour diagram is partly populated by post-AGB stars and it also has a connection to the bipolar post-AGB region (Zijlstra et al. 2001; Paper I). Further evidence that our particular objects are post-AGB stars will come from their spectral energy distributions (Section 4.2). Only the 25 sources with double-

<sup>1</sup>sevenste@strw.leidenuniv.nl

<sup>2</sup>A self-explanatory archive of all OH and IR data for 766 objects can be downloaded from <http://www.mso.anu.edu/~msevenster>

peaked OH spectra are used, to avoid the inclusion of star-forming regions (SFRs) in the sample and to be able to determine the outflow velocities. The LI stars are listed in Table 5.

The red group, “RI”, consists of 31 double-peaked sources with simply  $R_{32} < 1.5$  and  $R_{21} > 1.4$ . They are the “traditional” post-AGB sources (Bedijn 1987; van der Veen & Habing 1988), turned right from the evolutionary sequence into IRAS region V and beyond (see Fig. 2). They are listed in Table 6. The LI sources have higher outflow velocities than the RI sources (Fig. 1). The latter in fact stand out as a separate group with outflow velocities between  $9 \text{ km s}^{-1}$  and  $15 \text{ km s}^{-1}$  (Paper I). The LI sources do not only have relatively red  $R_{32}$  but also very red  $R_{43}$  as seen in Fig. 2. Otherwise, these sources are very blue, as will be substantiated in the next sections.

### 3. EVOLUTION

#### 3.1. Colours

In Fig. 3 we present MSX colour diagrams with symbols according to IRAS properties. Sources that are still close to the IRAS evolutionary sequence already show changes in MSX colours (‘x’ in Fig. 3a,c). The MSX colour  $[12 - 21]$  also increases suddenly for the reddest sources, but  $[12 - 15]$  is very constant (Fig. 3b). In Fig. 3d, the combined colour  $R_{21}^{ea} = 2.5 \log((S_{21}^{msx} S_{12}^{iras}) / (S_8^{msx} S_{25}^{iras}))$  shows a very marked increase at  $R_{21} = 1.2 \pm 0.2$  (see also Fig. 3c). The jump occurs as soon as sources redden in  $[8 - 12]$  (see Fig. 3a) and the subsequent increase in  $[15 - 21]$  keeps this colour constant with increasing  $R_{21}$ . It is also the best MIR diagnostic to separate (OH-masing) SFRs with  $R_{21}^{ea} < 0.9$  from (evolved) post-AGB objects with  $R_{21}^{ea} > 0.9$  (Fig. 3d). In other infrared colours, these two groups of sources show considerable overlap (see Paper I).

It seems likely that the sources at  $R_{21} \sim 1.2$  with high  $R_{21}^{ea}$  are the earliest post-AGB stars (cf. Paper I). The limits in  $R_{21}$  of this sudden transition correspond to  $R_{32} = -0.6$  and  $R_{32} = 0.71$  on the evolutionary sequence (Equation 1). It is thought that after the AGB, the “standard” (RI) sources evolve at fairly constant  $R_{32}$  toward redder  $R_{21}$ , as shown by Bedijn (1987). For higher mass-loss rate (Bedijn 1987) and thus higher initial mass (Likkell 1989; Garcia-Lario et al. 1993), the turn-off  $R_{32}$  is higher. The  $R_{32}$  limits mentioned above translate into  $M_i \sim 1 M_\odot$  and  $M_i \sim 4 M_\odot$  ( $< M_i > = 1.7 M_\odot$  for an IMF with  $\alpha = 2.5$ ), following Garcia-Lario et al. (1993). Now evolved to higher  $R_{21}$ , the RI sources would all come from this same mass range.

The LI sources do not fit in this scenario, nor do they show the colour jump in Fig. 3d. Rather, they are even bluer than the evolutionary-sequence sources in some colours. If these sources are indeed post-AGB sources (Section 2), they must evolve in a very different way from the RI sources. They have average  $[15 - 21] = 0.1$  (0.2 for full sample, 1.1 for RI; Fig. 3(a)) but  $[12 - 15] = 0.4$  (0.3 and 0.9; Fig. 3(b)). This  $15\text{-}\mu\text{m}$  excess can be understood in terms of a spectrum with blue continuum and strong silicate absorption at  $10\text{-}\mu\text{m}$  as well as  $18\text{-}\mu\text{m}$ . Comparing to the recent assesment of low-resolution spectra by Chen et al. (2001), we find that in the LI region of the IRAS diagram indeed spectra are mostly of their type “A”, which is the same as the traditional type “3n” of the low-resolution spectral associations (see IRAS Explanatory Supplement).

This indicates high mass-loss rates and thus high initial masses (eg. Bedijn 1987). More discussion of the spectral energy distribution will follow in Section 4.

#### 3.2. Model tracks

A number of post-AGB evolution tracks can be found in the literature. Unfortunately, a lot of assumptions still have to be made, most significantly about the evolution of the outflow velocity and the exact time of the “end” of the AGB. These quantities are frequently kept constant, while varying other parameters, such as initial mass. Van Hoof et al. 1997 (HOW97), however, vary those quantities for a range of models with initial mass  $3 M_\odot$ . Some of their tracks are shown in the IRAS two-colour diagram (Fig. 4) and in the combined near-mid-infrared two-colour diagram (Fig. 5; HOW97).

The dashed curves in both figures are for models with (+) silicate dust formation in the post-AGB outflow, the solid curves for models without (−). The numbers indicate the post-AGB outflow velocity assumed in the corresponding model ( $15 \text{ km s}^{-1}$  or  $150 \text{ km s}^{-1}$ ; the preceding AGB outflow velocity is  $15 \text{ km s}^{-1}$  for both). The third variable is AGB termination: either “early” (at period 125 days) or “standard” (at period 100 days, see HOW97 for details). Hence we have models 15−, 15+, 150+, 150+(early), etc.

Both post-AGB dust formation and early AGB termination cause sources to “loop” back to very blue  $R_{21}$  before resuming steady evolution toward higher  $R_{21}$ . The 15+ model loops into region VIII (see Fig. 2), but not to the left of the evolutionary sequence. To reach such low  $R_{21}$  during the post-AGB evolution, it appears that early AGB termination is a must. Although HOW97 did not give this model, by extrapolation it seems that the 15+(early) track could possibly explain the IRAS colours of the LI sources. The same holds for the colours in the combined infrared diagram (Fig. 5), where the 15+(early) track would dip down at fairly constant  $K - [12]$  to where the few LI sources with available NIR colours can be found. The evolution around the “turn-around” tip of the tracks may be rather slow, so relatively many sources would be found with those colours.

It should be noted that Steffen et al. (1998) also present models that “loop” through the IRAS two-colour diagram. These are evolutionary models for AGB stars in the thermally pulsing phase, however, that undergo episodes of interrupted mass loss (Zijlstra et al. 1992). Those objects have similar  $60\text{-}\mu\text{m}$  excess to our LI stars, but much bluer  $R_{21}$ , and are located to the left of region VIIb (Fig. 2).

Given our findings in Paper I, it seems probable that the outflow velocity does not increase significantly during the initial post-AGB phase – as long as  $1612\text{-MHz}$  masers are present – and that the  $15\text{-km s}^{-1}$  models are the proper ones for both RI and LI sources. It is hard to draw any conclusions about the importance of dust formation in the post-AGB outflow in the absence of models for a proper range of initial masses, but there is clear evidence that both the standard and the early AGB termination models may be realistic. The discussion in Section 3.1 would favour the 15− model for the RI sources, with continuous  $R_{21}$  reddening at fairly constant  $R_{32}$ , and more evidence for this will be presented in the Section 4.1.

For the values of  $R_{21}$  out to which we see the OH masers, the HOW97 models suggest that OH masers might disap-

pear around  $T_{\text{eff}}=6500\text{ K}$ , both for the RI sources (standard termination) and for the LI sources (early). For the standard models, this temperature is reached within 500 yr of leaving the AGB, for the early models only after 5000 yr. Hence, for these particular models of AGB termination, the LI sources would spend ten times longer being OH-masing post-AGB objects than the RI sources.

#### 4. SPECTRAL ENERGY DISTRIBUTION

The spectral energy distributions (SED) are shown for the RI and LI sources with the most complete spectral coverage by IRAS, MSX and 2MASS (Fig. 6). For reference, two sources on the AGB evolutionary sequence are shown as well. The location of the sources in the IRAS two-colour diagram and their outflow velocity are shown in the insert. The outflow velocities of the selected LI and RI sources are as expected (Fig. 1).

The first thing to notice in Fig. 6 is that the ratio of the IRAS 12- $\mu\text{m}$  to the MSX 12- $\mu\text{m}$  flux density gives an indication of whether the 9.7- $\mu\text{m}$  silicate feature is in emission (bluer AGB source) or in absorption (redder AGB source); indeed this is as typically expected. The SED of the LI sources is very similar to those of the AGB sources, but has even redder NIR distribution and a strong 60- $\mu\text{m}$  excess as noted in Section 3.1. Also, they have a weak 15- $\mu\text{m}$  excess, compared to the AGB sources, and the silicate feature seems to be in absorption. The RI sources clearly stand out with bluer NIR and, by definition, redder distributions between 10 and 25  $\mu\text{m}$ . The silicate feature appears to be mostly in emission.

##### 4.1. Comparison to model spectra

Comparing the SEDs to the model spectra by Bedijn (1987), the two AGB sources (#1& #2) have mass-loss rates of a few times  $10^{-6}\text{ M}_{\odot}\text{ yr}^{-1}$ . For the LI sources (#3& #4) no suitable model is found, since Bedijn did not consider that region of the IRAS two-colour diagram, but for the RI sources, the post-AGB models offer a good explanation. The NIR colours should correlate strongly with the time since AGB termination, with the colours becoming bluer with time. The NIR-to-MIR flux-density ratio increases faster for sources with lower AGB mass-loss rates and thus lower initial masses.

From the comparison between the spectral energy distributions and Bedijn's models, we estimate that the RI sources (#5 - #10) plotted in Fig. 6 had AGB mass-loss rates of  $10^{-4}$  to  $10^{-3}\text{ M}_{\odot}\text{ yr}^{-1}$  and all left the AGB less than  $\sim 500$  yr ago. The RI sources #9 and #10 already have strong NIR - very blue J-K - but still low NIR-to-MIR flux-density ratio. This suits the models with higher mass loss ( $10^{-3}\text{ M}_{\odot}\text{ yr}^{-1}$ ), in agreement with the idea that higher-mass sources have larger turn-off  $R_{32}$  (Section 3.1). It is also in agreement with the idea that sources evolve off the AGB toward redder  $R_{21}$  at almost constant  $R_{32}$ .

##### 4.2. Comparison to observed spectra

Van der Veen et al. (1989) give 5 observational classes of post-AGB SEDs. The LI sources (#3& #4 in Fig. 6) are clearly of "class I". Of the five class-I sources in van der Veen et al. (1989), three are located in IRAS regions IV and VIII to the left of the evolutionary sequence. The RI sources (#5 - #10 in Fig. 6) are all "class IVa". According to van der Veen et al. (1989), there is a large difference

in initial mass between the two classes :  $4\text{ M}_{\odot}$  for class I and  $1.7\text{ M}_{\odot}$  for class IVa (from luminosity-distance self-consistency arguments). This is in excellent agreement with our derived mass range of  $1-4\text{ M}_{\odot}$  for the RI sources and the fact that the LI sources could be the more massive (higher mass loss) sources (Section 3.1). Other properties of the post-AGB groups are in Table 1; both classes have a high percentage of O-rich objects. The class-I sources, hence the LI stars, would still have considerable mass loss (van der Veen et al. 1989).

#### 5. PRECURSORS AND SUCCESSORS

Since the LI sources have higher outflow velocities than the RI sources, the first assumption is that they have higher luminosities and/or metallicity (van der Veen 1989). Clearly, we already found indications that the LI sources are more massive in Section 3.1&4. Our observations could be explained, if the "early" transitions of the HOW97 models (Section 3.2) were to happen only in the more massive objects.

In an attempt to trace further intrinsic differences between the two groups of stars, we first determined the average latitude of the 25 LI sources,  $0^{\circ}46$ , and of the 31 RI sources,  $1^{\circ}66$  (Fig. 7, Table 3). Average latitude, or angular vertical scale, is directly proportional to the absolute vertical scale,  $h_z$ , of a sample and inversely to average distance. Itself,  $h_z$  is a function of the age  $t$  of the sample, via the vertical velocity dispersion  $\sigma_w$ . The dispersion increases as  $\sigma_w \propto t^{0.5}$  (Wielen 1977, for stars from 0.2 Gyr to 5 Gyr; Just et al. 1996). Close to the plane,  $h_z \propto \sigma_w$  and out of the plane  $h_z \propto \sigma_w^2$  (Just et al. 1996). For the LI group,  $h_z \propto t^{0.5}$  is definitely appropriate (Fig. 7). For the RI sample, reaching out to latitudes well over  $3^{\circ}$  (Fig. 7), the exponential is possible larger than 0.5 (and smaller than 1). All in all, the LI sources are either much younger than the RI sources or much further away.

Second, the stellar luminosities should be roughly proportional to  $V_{\text{exp}}^4$  for similar metallicities :

$$L_* \propto V_{\text{exp}}^4 Z^{-2}, \quad (2)$$

following van der Veen (1989). So,  $L_*^{\text{LI}} \sim 3.2 L_*^{\text{RI}}$  (Table 3). This clearly fits in well with the previous argument that the LI sources should be much younger than the RI sources, if at similar distances.

Third, the average bolometric correction  $BC_{12}$  at 12  $\mu\text{m}$  for the RI sources is 5.3, for the LI sources 2.7 (van der Veen & Breukers 1989). The ratio of the total bolometric fluxes then would be  $S_{\text{bol}}^{\text{LI}}/S_{\text{bol}}^{\text{RI}} = (S_{12} * BC_{12})^{\text{LI}}/(S_{12} * BC_{12})^{\text{RI}} \sim 6.75/2 = 3.4$  on average.

From arguments 1+2, we can assume that the two groups are at similar distances, and from arguments 2+3 that they have similar metallicities. Hence, from the second argument, LI stars are three times more luminous than the RI stars and indeed originated from more massive main sequence stars.

So, let's assume that the LI sources had average initial masses of  $4\text{ M}_{\odot}$  and the RI sources  $1.7\text{ M}_{\odot}$  (see Table 1). Corresponding AGB-tip luminosities and ages (Bertelli et al. 1994) are in Table 3. The luminosities are a factor of two higher than those given in Table 1. The latter are current, post-AGB luminosities, whereas the former are

TABLE 1

DETAILS FOR POST-AGB CLASSES I AND IVa FROM VAN DER VEEN ET AL. (1989; SEE SECTION 4.2). THE  $\dot{M}_p$  STANDS FOR PRESENT POST-AGB MASS LOSS AND O FOR THE FRACTION OF OXYGEN-RICH SOURCES IN BOTH CLASSES.

	$M_i$	$M_c$	L	$h_z$	O	$\log(\dot{M}_p)$
Class I	4	0.8	15000	85	60	-5
Class IVa	1.7	0.6	5000	250	80	-7

TABLE 2

DETAILS FOR THE SOURCES IN FIG. 6. THE  $S_{\text{OH}}$  IS FOR THE STRONGEST 1612-MHz PEAK,  $S_{25}$  FROM IRAS.

#	Name (OH $\ell$ , $b$ )	IRAS	$V_{\text{exp}}(\frac{\text{km}}{\text{s}})$	$S_{\text{OH}}(\text{Jy})$	$S_{25}(\text{Jy})$	K
1	OH355.588−02.978	17434−3414	6.6	0.44	41.91	4.82
2	OH350.982−02.391	17288−3748	14.6	1.38	26.63	5.04
3	OH344.929+00.014	17004−4119	19.0	39.93	322.60	−
4	OH010.076−00.095	18052−2016	28.5	2.02	32.45	7.57
5	OH355.641−01.742	17385−3332	10.2	4.03	13.25	9.07
6	OH359.140+01.137	17359−2902	9.5	1.66	12.38	10.40
7	OH001.212+01.257	17404−2713	13.1	4.48	20.74	11.08
8	OH353.945−00.972	17310−3432	11.7	1.39	10.85	11.47
9	OH353.973+02.727	17164−3226	13.9	2.33	9.45	12.78
10	OH007.961+01.445	17550−2120	12.4	4.30	21.08	13.22

TABLE 3

MEASURED AVERAGES AND MODEL VALUES ( $M_i$  AS ASSUMED; COLUMNS 5,6 FOR AGB-TIP AND  $Z=0.02$  FROM BERTELLI ET AL. 1994).

	$\langle V_e \rangle$	$\langle b \rangle$	$\langle S_{12,25,60} \rangle$	$M_i$	t	$L_*$
	km/s	$^\circ$	Jy	$M_\odot$	Gyr	$L_\odot$
RI	13.1	1.66	4,25,29	1.7	1.8	1.0E4
LI	17.5	0.46	28,68,88	4.0	0.2	3.2E4

TABLE 4

MEASURED AND PREDICTED RATIOS (LI/RI)

	$L_*$	$\langle b \rangle$	$S_{\text{OH}}$
predicted	$\sim 3.0$	$\lesssim 0.33$	$\sim 0.4$
measured	$3.3 \pm 0.1$	$\lesssim 0.28$	$\sim 0.5$

TABLE 5  
DETAILS FOR THE LI SOURCES. THE  $S_{\text{OH}}$  IS FOR THE HIGHEST PEAK.

Name (OH $\ell$ , $b$ )	IRAS	$V_{\text{exp}}(\frac{\text{km}}{\text{s}})$	$S_{\text{OH}}(\text{Jy})$
OH326.518−00.633	15452−5459	9.5	9.27
OH328.225+00.042	15514−5323	19.7	57.78
OH344.929+00.014	17004−4119	19.0	39.93
OH351.592+00.318	17193−3546	10.2	0.78
OH351.607+00.022	17205−3556	18.3	0.33
OH351.118−00.352	17207−3632	16.8	1.36
OH353.637+00.815	17230−3348	9.5	2.77
OH354.642+00.830	17256−3258	32.8	0.58
OH358.425−00.175	17392−3020	21.2	1.00
OH357.988−00.988	17414−3108	14.6	0.55
OH010.076−00.095	18052−2016	28.5	2.02
OH007.452−02.615	18092−2347	17.0	0.20
OH011.522−00.582	18100−1915	13.6	1.10
OH012.973+00.133	18103−1738	21.5	0.80
OH016.117−00.291	18182−1504	21.5	9.40
OH020.679+00.084	18257−1052	18.2	5.80
OH021.457+00.491	18257−1000	18.1	18.90
OH022.993−00.285	18314−0900	14.8	8.30
OH024.692+00.235	18327−0715	19.3	4.40
OH025.495−00.288	18361−0647	15.9	1.80
OH030.715+00.427	18432−0149	17.0	3.90
OH030.554+00.281	18434−0202	19.2	1.10
OH030.091−00.686	18460−0254	19.2	35.10
OH031.984−00.485	18488−0107	19.3	5.10
OH038.101−00.125	18588+0428	21.5	0.40

the luminosities the objects would have had on the tip of the AGB. Post-AGB luminosities are also given by Vassiliadis & Wood (1994) and interpolate to  $\sim 6350 L_{\odot}$  and  $\sim 17000 L_{\odot}$  for those masses, both for H-burning and solar metallicity.

Importantly, the luminosity ratio between the two groups is  $3^{+0.2}_{-0.3}$  from all three references, compared to 3.2 from the outflow velocities or 3.4 from the bolometric fluxes. For  $< b > t^{>0.5}$ , the ratio of average latitudes would be  $\lesssim 0.33$ , compared to  $\lesssim 0.28$  from the observations. For the assumed initial masses, van der Veen (1989) gives AGB outflow velocities of  $13 \text{ km s}^{-1}$  and  $17 \text{ km s}^{-1}$ , respectively. All observed values are closely reproduced (Table 3). The median OH-peak flux density for the RI sample is twice that for the LI sample. This is close to what is expected from  $S_{\text{OH}} \propto S_{\text{bol}}^{1.5} X_{21}^2$  (Paper I, Equation 3b), giving a ratio of  $3.4^{1.5} * 0.25^2 \sim 0.4$ .

From a typical initial-mass function, we would expect about 10 times more sources between  $1\text{--}4 M_{\odot}$  than between  $4\text{--}6 M_{\odot}$  (the AGB limit). For our OH sample, however, the numbers are roughly equal. OH selection effects do not explain this discrepancy, since the OH luminosities of the RI sample are higher than those of the LI sample, if indeed the average distances to the two samples are the same, as argued above. From the model tracks by HOW97, however (see Section 3.2), the LI sources are expected to take much longer than the RI sources to reach an effective temperature of 6500 K after leaving the AGB (see Section 3.2). Since the effective temperature plays an important role in the termination of the OH masers, this effect could make up the numbers.

The  $60\text{-}\mu\text{m}$  flux-density measurements of the LI stars might be overestimated in the IRAS point-source catalogue due to their very low latitudes. However, using the available flags in the IRAS PSC, both the LI and the RI sources are found to be mostly in confused regions. The CIRR1 and CIRR2 flags average 6 to 7 for both groups and CIRR3 is 254 for all RI and LI sources (IRAS Explanatory Supplement). Thus, as mentioned in the introduction, it is likely that the  $60\text{-}\mu\text{m}$  fluxes are overestimated for all sources in our low-latitude survey, but the LI sources are not necessarily suffering more from this effect.

A mechanism that may cause different evolution at the tip of the AGB for different initial masses could be hot-bottom burning. Only AGB stars more massive than  $\sim 4 M_{\odot}$  undergo this process. This mass limit fits in very well with what we have found in this paper. In Fig. 2, an object is plotted that is argued to be hot-bottom burning (van Loon et al. 2001). It is IRAS 05298–6957, an LMC cluster OH/IR star. This object is indeed found to have the properties of an LI star. Its OH outflow velocity is  $11 \text{ km s}^{-1}$  (Wood et al. 1992) which is consistent with typical LI luminosity, for  $Z=0.008$  instead of 0.02.

### 5.1. Massive precursors to bipolar PN ?

It is interesting to revisit the scaleheights of the two groups (Fig. 7). Following Sevenster (1999), the apparent scaleheights deproject to roughly 100 pc and 300 pc,

respectively. Due to our narrow latitude coverage, the latter value may be somewhat underestimated. Those values are close to what van der Veen found for the two spectral classes (Table 1) and correspond closely to the scaleheights given by Corradi (2000) for bipolar (130 pc) and elliptical (320 pc) planetary nebulae. Also, the location of the “bipolar outflow” region defined by Zijlstra et al. (2001) suggests that the LI sources may be related to bipolar sources. The higher fraction of irregular spectra amongst LI sources and the preferred location of sources with irregular spectra in this “bipolar outflow” region, as found in Paper I, indicate that on their way “back” to the red PN region of the IRAS two-colour diagram the LI sources may go through a highly irregular, high-outflow mass-loss phase. The bipolar planetary nebulae themselves might again be located to the right of the evolutionary sequence (Fig. 4; HOW97), but no longer harbour OH masers. One would expect the average  $R_{32}$  of bipolar PNe to be higher than that of elliptical PNe, if this scenario were correct. This appears to be the case : Corradi & Schwarz (1995) show that for  $R_{21} \lesssim 2$  bipolars are located at  $0 \lesssim R_{32} \lesssim 2$  and ellipticals at  $-1 \lesssim R_{32} \lesssim 1$ , the same range as the RI sources.

## 6. CONCLUSIONS

A red and a blue group of OH-masing post-AGB stars are discussed in detail. The consistency of a variety of independent arguments provides a solid basis for the assumption that the blue sources are indeed post-AGB objects; their existence was predicted by van Hoof et al. (1997). Using evolutionary-sequence turn-off colours, spectral energy distributions, outflow velocities and scale-height, we argue that the two groups separate by initial mass at  $M_i = 4 M_{\odot}$ .

The higher-mass objects may have AGB termination earlier (at still longer periods) than the lower-mass objects and make a blue- $R_{21}$  loop through the IRAS two-colour diagram. They have a  $15\text{-}\mu\text{m}$  excess, as well as strong  $60,100\text{-}\mu\text{m}$  excess. The lower-mass objects show very sudden reddening at  $R_{21} \sim 1.2$ , which corresponds to average initial masses of  $\sim 1.7 M_{\odot}$ . These sources must all undergo a very similar process at AGB termination.

At the end of their OH-masing post-AGB stages, the high-mass, blue objects may go through an irregular mass-loss phase (Paper I), preceding the bipolar planetary-nebulae stage. The low-mass, red objects probably evolve into elliptical planetary nebulae.

The combined colour  $2.5 \log((S_{21}^{\text{msx}} S_{12}^{\text{iras}})/(S_8^{\text{msx}} S_{25}^{\text{iras}}))$  proves very sensitive to distinguish lower-mass, early post-AGB objects from sources still on the AGB and also to distinguish more evolved post-AGB objects from star-forming regions.

MS thanks Peter van Hoof for making the model tracks available and offering useful comments about this paper. The Leidse Sterrewacht kindly provided desk and computer to finish the final version of this paper.

TABLE 6  
DETAILS FOR THE RI SOURCES. THE  $S_{\text{OH}}$  IS FOR THE HIGHEST PEAK.

Name (OH $\ell$ , $b$ )	IRAS	$V_{\text{exp}}(\frac{\text{km}}{\text{s}})$	$S_{\text{OH}}(\text{Jy})$
OH314.933−02.052	14341−6211	9.5	0.64
OH335.832+01.434	16209−4714	13.9	1.23
OH338.507−02.915	16507−4810	11.7	0.62
OH349.949+01.537	17097−3624	12.4	0.70
OH353.973+02.727	17164−3226	13.9	2.33
OH349.804−00.321	17168−3736	13.1	10.89
OH348.813−02.840	17245−3951	11.7	13.09
OH353.945−00.972	17310−3432	11.7	1.39
OH359.750+02.629	17317−2743	11.0	4.60
OH359.140+01.137	17359−2902	9.5	1.66
OH355.111−01.697	17370−3357	11.7	2.77
OH355.641−01.742	17385−3332	10.2	4.03
OH000.892+01.342	17393−2727	14.6	47.87
OH001.212+01.257	17404−2713	13.1	4.48
OH359.233−01.876	17479−3032	13.1	1.94
OH004.007+00.915	17482−2501	14.6	1.25
OH000.072−02.044	17506−2955	10.9	0.76
OH002.286−01.801	17548−2753	16.1	1.42
OH007.961+01.445	17550−2120	12.4	4.30
OH008.854+01.689	17560−2027	13.6	3.00
OH004.017−01.679	17582−2619	11.0	1.02
OH006.594−02.011	18051−2415	13.6	0.40
OH015.364+01.925	18087−1440	14.8	3.40
OH015.700+00.770	18135−1456	14.8	9.60
OH017.684−02.032	18276−1431	11.4	39.00
OH025.057−00.350	18355−0712	11.4	2.80
OH027.577−00.853	18420−0512	12.4	3.00
OH030.394−00.706	18467−0238	27.2	0.60
OH038.909+03.178	18485+0642	13.6	11.50
OH037.118−00.847	18596+0315	13.6	6.60
OH035.209−02.653	19024+0044	13.6	4.00

## REFERENCES

- Bedijn P., 1987, A&A, 186, 136  
 Bertelli G., Bressan A., Chiosi C., Fagotto F., Nasi E., 1994, A&AS, 106, 275  
 Caswell J., 1998, MNRAS, 297, 215  
 Caswell J., 1999, MNRAS, 308, 683  
 Chen P., Szczerba R., Kwok S., Volk K., 2001, A&A, 368, 1006  
 Corradi R., Schwarz H., 1995, A&A, 293, 871  
 Corradi R., 2000, In: Kastner J., Soker N., Rappaport S. (eds.) Asymmetric Planetary Nebulae II. ASP Conf.Ser.199 p. 25  
 Garcia-Lario P., Manchado A., Pottasch S., 1993, In: Planetary Nebulae (eds. Weinberger, Acker) IAU 155 Kluwer, Dordrecht p.332  
 Just A., Fuchs B., Wielen R., 1996, A&A, 309, 715  
 Likkell L., 1989, ApJ, 344, 350  
 Sevenster M., Chapman J., Habing H., Killeen N., Lindqvist M., 1997a, A&AS, 122, 79  
 Sevenster M., Chapman J., Habing H., Killeen N., Lindqvist M., 1997b, A&AS, 124, 509  
 Sevenster M.N., 1999, MNRAS, 310, 629  
 Sevenster M.N., 2002, AJ, 00, 000 (Paper I)  
 Sevenster M., van Langevelde H., Moody R., Chapman J., Habing H., Killeen N., 2001, A&A, 366, 481  
 Steffen M., Szczerba R., Schönberner D., 1998, A&A, 337, 149  
 van der Veen W., Habing H., 1988, A&A, 194, 125  
 van der Veen W., 1989, A&A, 210, 127  
 van der Veen W., Breukers R., 1989, A&A, 213, 133  
 van der Veen W., Habing H., Geballe T., 1989, A&A, 226, 108  
 van Hoof P., Oudmaijer R., Waters L., 1997, MNRAS, 289, 371 (HOW97)  
 van Loon J., Zijlstra A., Kaper L., Gilmore G., Loup C., Blommaert J., 2001, astro-ph 0101107  
 Vassiliadis E., Wood P., 1994, ApJS, 92, 125  
 Wielen R., 1977, A&A, 60, 263  
 Wood P., Whiteoak J., Hughes S., Bessell M., Gardner F., Hyland A., 1992, ApJ, 397, 552  
 Zijlstra A., Loup C., Waters L., de Jong T., 1992, A&A, 265, L5  
 Zijlstra A., Chapman J., Te Lintel Hekkert P., Likkell L., Comeron F., et al. 2001, MNRAS, 322, 280



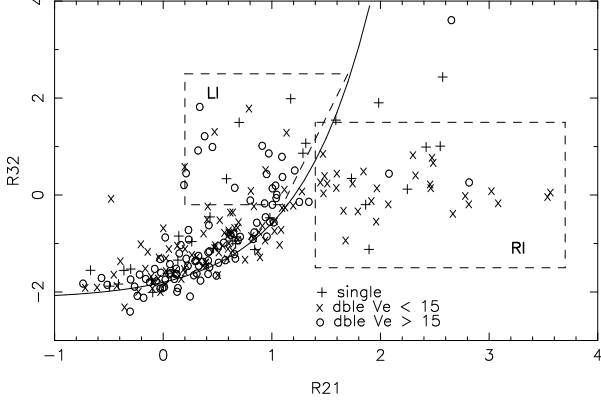


FIG. 1.— The IRAS two-colour diagram with symbols according to outflow velocity. The “standard” post-AGB region to the right of the evolutionary sequence (“RI” sources) is populated mostly by sources with outflow velocities below  $15 \text{ km s}^{-1}$ . In the region to the left, on the other hand, sources have mostly higher outflow velocities (“LI” sources).

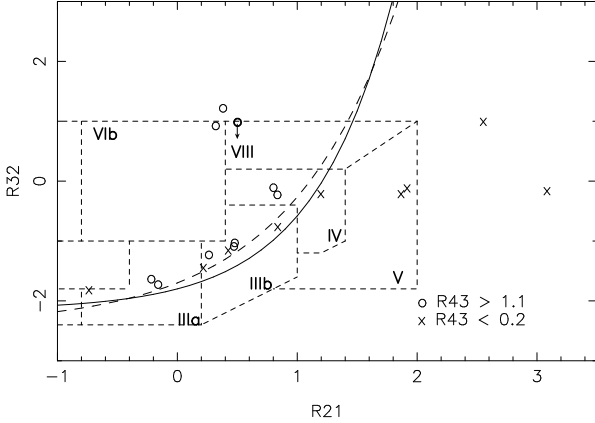


FIG. 2.— The IRAS two-colour diagram showing the sources selected by  $R_{43}$  ([60–100]). Only very few sources have well-defined  $S_{100}$ , but the “LI” and “RI” (Section 2) branches clearly stand out, in an exaggerated way, in this selection. Be aware that the  $100\text{-}\mu\text{m}$  flux-density measurements are most likely to be overestimated for the LI sources, as they are close to the Plane (see Section 5). The fat circle with arrow indicates the hot-bottom-burning OH/IR star in the LMC (van Loon et al. 2001) discussed in Section 5. The solid curve is the theoretical evolutionary sequence (Equation 1), the dashed curve is a common observational evolutionary sequence ( $R_{32} = -2.42 + 0.72 \exp[1.1 R_{21}]$ ). The dashed boxes are the regions as defined in Van der Veen & Habing (1988).

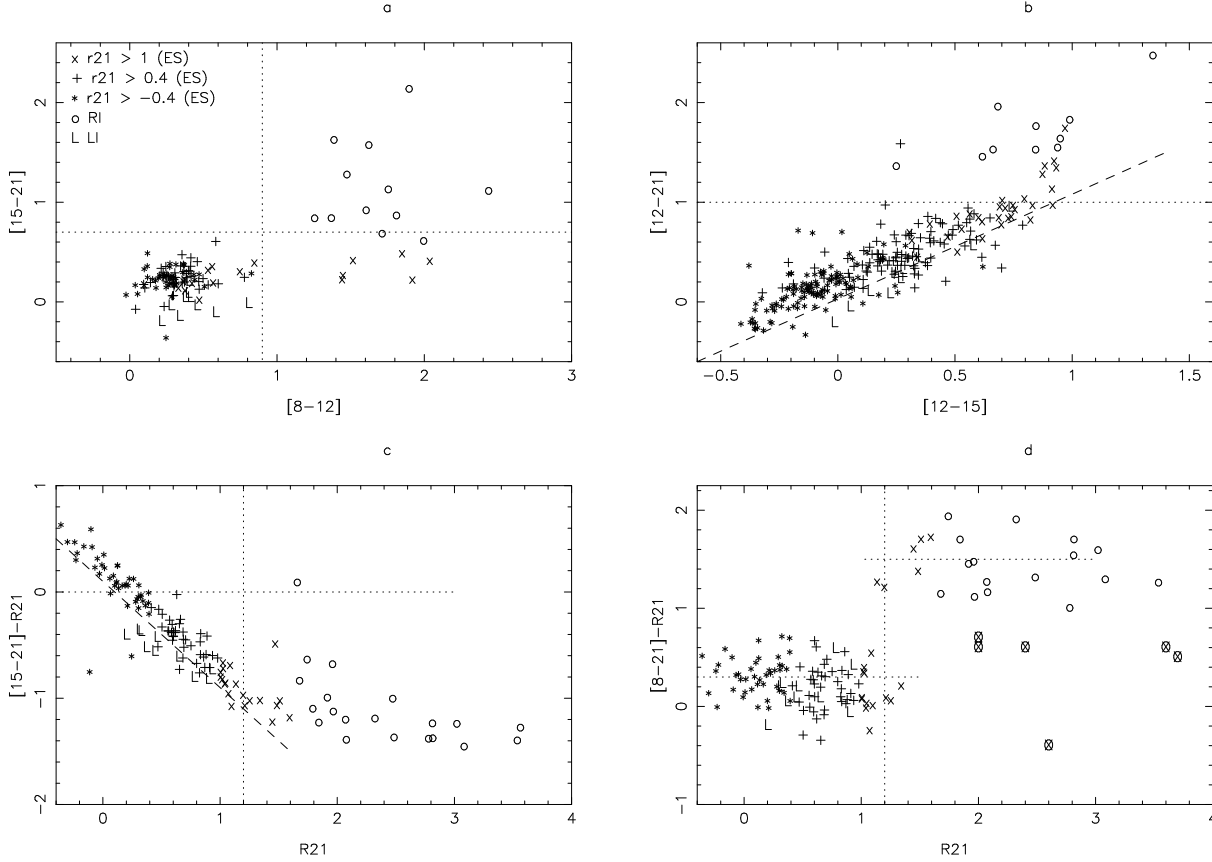


FIG. 3.— The top panels (a,b) show two MSX two-colour diagrams and the bottom panels (c,d) plot the IRAS colour  $R_{21}$  versus the difference between MSX colours and  $R_{21}$ . In all panels, only double-OH-peaked sources are plotted, with symbols according to IRAS colours : (\*,+,x) for sources close to the evolutionary sequence with increasing  $R_{21}$ , as well as the LI ('L') and RI ('o') sources as defined in Section 2. The LI sources clearly have the bluest  $[15 - 21]$  of all and slightly redder  $[12 - 15]$  than the bulk of the AGB sources. The MSX colour  $[8 - 21]$  is the best equivalent of  $R_{21}$ . They are almost equal for  $R_{21} < 1.2$  ( $T=170$  K) and  $[8 - 21]$  is four times redder for  $R_{21} > 1.2$ . The transition is very sudden transition and corresponds to an average initial mass of  $1.7 M_{\odot}$  (Section 3.1). In plot d, some known OH-masing star-forming regions (Caswell 1998,1999) are plotted for reference (encircled crosses). Dashed and dotted lines in all panels are plotted to guide the eye. This figure is discussed in detail in Section 3.1.

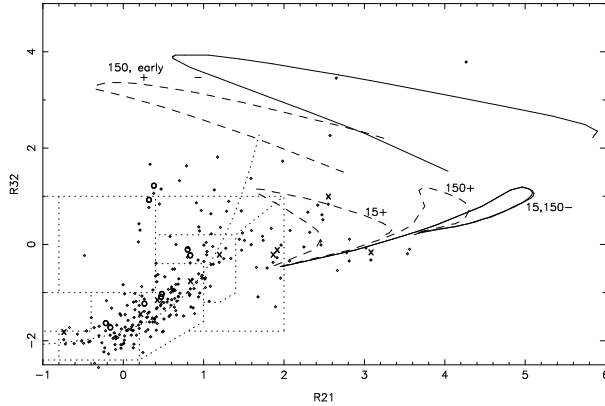


FIG. 4.— The IRAS two-colour diagram, with all objects indicated by dots and circles and crosses as Fig. 2. Overlaid are  $3-M_{\odot}$  tracks from HOW97, for post-AGB wind of  $15 \text{ km s}^{-1}$  and  $150 \text{ km s}^{-1}$  with (dashed) and without (solid) post-AGB dustformation. For  $150 \text{ km s}^{-1}$ , there are also the models for early AGB termination. A “15+(early)” model would possibly reach in to the regions where the LI sources are found.

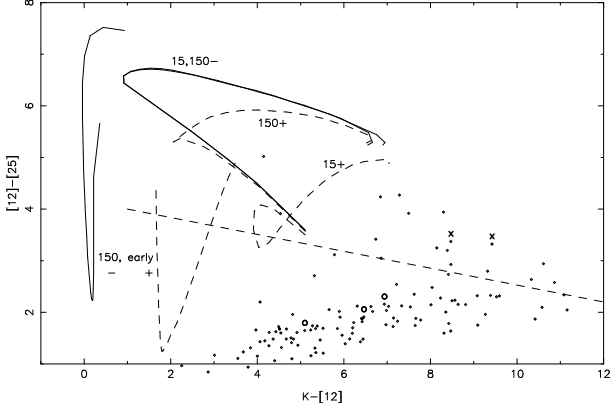


FIG. 5.— The mid-near-infrared colour diagram as advocated by HOW97, with tracks as in Fig. 4. Circles indicate LI sources, crosses are sources with  $R_{43} < 0.2$  (Fig. 2). Note that the circles and crosses are not the same selection as in Fig. 4, but do indicate similar sources. The dashed line separates the RI sources from the (bluer) AGB sources. The tracks are calculated for a distance of 1 kpc. As the sources are mostly well further than that, they can be dereddened by moving them to lower  $K-[12]$  (hardly any reddening for  $[12]-[25]$ ). Again, a “15+(early)” model might be the best candidate to reproduce the (blue) colours of the LI sources.

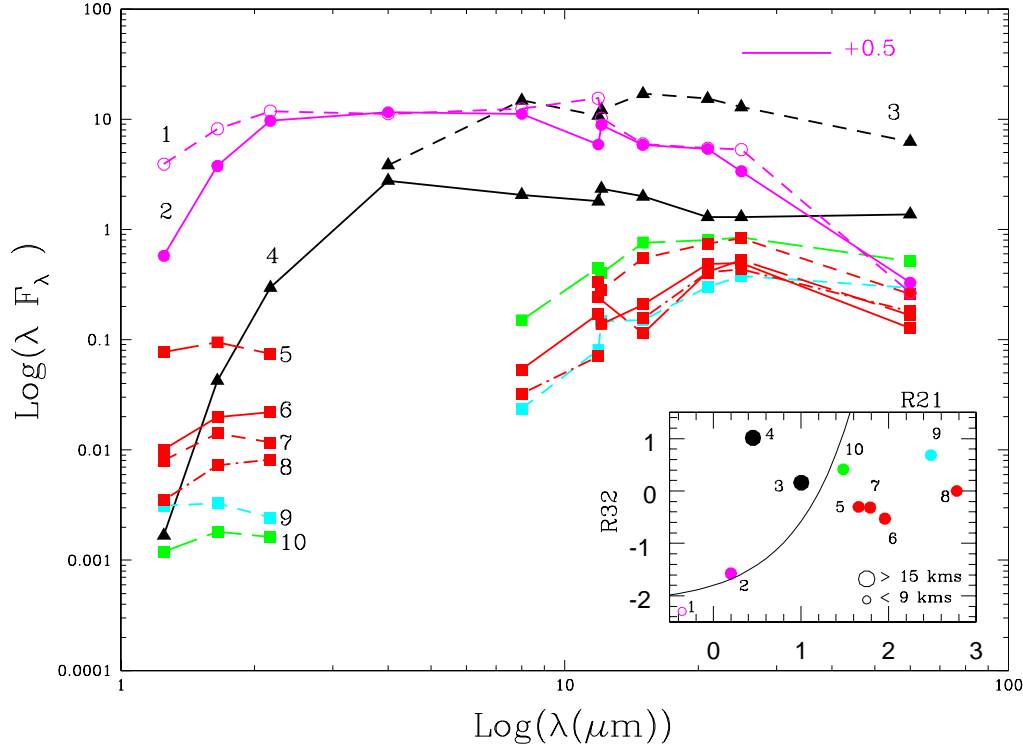


FIG. 6.— The spectral energy distributions composed of the flux densities in the NIR bands (2MASS) and the MIR bands (MSX, IRAS) for 2 AGB sources (#1&#2,cyan), 2 LI sources (#3&#4,black) and 6 RI sources (#5–#10,red,green,turquoise). The IRAS 12- $\mu\text{m}$  flux densities, including the 9.7- $\mu\text{m}$  silicate feature, is plotted slightly to the left of the MSX 12- $\mu\text{m}$  measurement, that does not include 9.7  $\mu\text{m}$ . The difference between the two may give an indication of the optical depth in the silicate feature. The inserted plot shows the location of the sources in the IRAS two-colour diagram, with symbol sizes scaled according to outflow velocity: smallest is  $V_{\text{exp}} < 9 \text{ km s}^{-1}$ , largest is  $V_{\text{exp}} > 15 \text{ km s}^{-1}$  and intermediate is in between. The open symbol in the insert corresponds to the SED with open symbols in the main plot. For the RI sources, the MSX 4- $\mu\text{m}$  flux densities are undetermined and some other points are missing in several of the SEDs. The AGB SEDs (#1&#2, cyan) are shifted upward by half a magnitude to avoid confusing overlap with the LI SED. The vertical axis is in arbitrary units.

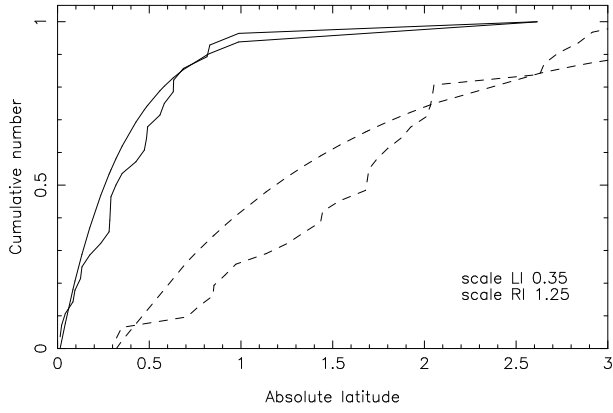


FIG. 7.— The cumulative distributions versus absolute latitude for the LI (solid) and RI (dashed) stars. The Kolmogorov–Smirnov probability that the two distributions are the same is  $3 \times 10^{-9}$ . The smooth fits are exponentials with apparent scaleheights  $0.35$  (100 pc) and  $1.25$  (300 pc), respectively (see Section 5.1 and compare to Table 1).